

# Online 3D Characterization of Micrometer-Sized Cuboidal Particles in Suspension

Pietro Binel, Ankit Jain, Anna Jaeggi, Daniel Biri, Ashwin Kumar Rajagopalan, Andrew J. deMello, and Marco Mazzotti\*

Characterization of particle size and shape is central to the study of particulate matter in its broadest sense. Whilst 1D characterization defines the state of the art, the development of 2D and 3D characterization methods has attracted increasing attention, due to a common need to measure particle shape alongside size. Herein, ensembles of micrometer-sized cuboidal particles are studied, for which reliable sizing techniques are currently missing. Such particles must be characterized using three orthogonal dimensions to completely describe their size and shape. To this end, the utility of an online and in-flow multiprojection imaging tool coupled with machine learning is experimentally assessed. Central to this activity, a methodology is outlined to produce micrometer-sized, non-spherical analytical standards. Such analytical standards are fabricated using photolithography, and consist of monodisperse micro-cuboidal particles of user-defined size and shape. The aforementioned activities are addressed through an experimental framework that fabricates analytical standards and subsequently uses them to validate the performance of our multiprojection imaging tool. Significantly, it is shown that the same set of data collected for particle sizing can also be used to estimate particle orientation in flow, thus defining a rapid and robust protocol to investigate the behavior of dilute particle-laden flows.

materials (e.g., metal–organic frameworks) and catalysts, and the production of pharmaceutical, agrochemical, and food compounds. In all situations, particle sizing plays a key role in the design and control of particle properties and particle size and shape manipulation.

Conventionally, a single characteristic length is used to describe particles, assuming a spherical geometry, or taking advantage of the concept of equivalent diameter. This assumption may be acceptable for irregular yet compact shapes, and is an established simplification functional to the description of various physical phenomena.<sup>[1]</sup> However, it is clearly incorrect when analyzing elongated or plate-like particles, i.e., with low sphericity, which are common crystalline products.<sup>[2]</sup> This leads to particle size and shape estimates that poorly match physical reality.<sup>[3–5]</sup> To describe both size and shape, at least two characteristic lengths are needed, which can be obtained through a number of 2D or 3D characterization techniques.<sup>[6–9]</sup>

## 1. Introduction

Accurate particle sizing is fundamental to many areas of scientific and industrial research, including the synthesis of porous

Such (offline and online) techniques, including micro-computed tomography ( $\mu$ CT),<sup>[10–17]</sup> holography,<sup>[18–20]</sup> structural light,<sup>[21]</sup> machine vision,<sup>[13,22–31]</sup> confocal microscopy,<sup>[32]</sup> and surface imaging<sup>[33]</sup> have varying degrees of accuracy and complexity. Machine vision through image analysis (IA) has become an increasingly powerful tool, due to experimental simplicity, hardware improvements, and continual increases in available computational power.<sup>[8]</sup>

For the online measurement of elongated, needle-like particles on the microscale, effective IA algorithms have been proposed and successfully used to track particle length and width distributions. This has enabled a better fundamental understanding of processes in particle technology.<sup>[34–38]</sup> By contrast, an experimentally validated methodology enabling the rapid and online measurement of cuboidal or plate-like particles has yet to be developed. Full 3D characterization is possible through  $\mu$ CT, but this comes with several downsides, such as extended scanning times and, in the case of powders, difficulties in particle segmentation.<sup>[14]</sup> 2D characterization by single projection imaging can be fast, but does not provide sufficient information to reliably extract characteristic lengths and shapes, whilst the accuracy of multiple projection imaging is compromised by particle orientation.<sup>[6,8]</sup> Other techniques, such as holography or surface imaging, are yet to be applied to, or are unsuited for online measurement purposes.

P. Binel, A. Jaeggi, D. Biri, M. Mazzotti  
Institute of Energy and Process Engineering  
ETH Zurich  
8092 Zurich, Switzerland  
E-mail: marcom@ethz.ch

A. Jain, A. J. deMello  
Institute for Chemical and Bioengineering  
ETH Zurich  
8093 Zurich, Switzerland

A. K. Rajagopalan  
Department of Chemical Engineering  
The University of Manchester  
Manchester M13 9PL, UK

 The ORCID identification number(s) for the author(s) of this article can be found under <https://doi.org/10.1002/smt.202201018>.

© 2022 The Authors. Small Methods published by Wiley-VCH GmbH. This is an open access article under the terms of the Creative Commons Attribution-NonCommercial-NoDerivs License, which permits use and distribution in any medium, provided the original work is properly cited, the use is non-commercial and no modifications or adaptations are made.

DOI: 10.1002/smt.202201018

**Table 1.** Populations of particles employed in the study.

AR $L_2/L_3$	AR $L_1/L_2$	Length $L_1$	Width $L_2$	Thickness $L_3$
3	1	100	100	33
	2	200	100	33
	3	300	100	33
1.5	2	200	100	66
	3	300	100	66
1	2	200	100	100
	3	300	100	100

Values of  $L$  in  $\mu\text{m}$ ; AR = aspect ratio.

Finally, and most importantly, the lack of cuboidal-shaped analytical standards means that a rigorous validation of any of these measurement techniques is currently not possible.

Accordingly, the goals of the current study are twofold:

- to show how monodisperse populations of arbitrarily shaped micrometer-sized cuboidal particles can be fabricated by photolithography and employed as novel analytical standards;
- to experimentally demonstrate how a multiprojection imaging device<sup>[39]</sup> coupled with a machine learning (ML) algorithm<sup>[40]</sup> is able to yield online and accurate estimates of the three characteristic lengths of such cuboidal particles in suspension.

Additionally, and by virtue of the information provided by two cameras during analysis of the suspensions, we are able to systematically investigate the effect of particle shape on the dynamics and orientations of particles. Moreover, the availability of particles of controlled size and shape allows for the validation of multiphase CFD simulations, which are relevant to a number of fields.<sup>[41–44]</sup>

## 2. Experimental Section

To cover a broad range of sizes and aspect ratios, seven populations of cuboidal particles were fabricated, each consisting of 10 000–15 000 particles. Three ratios of width to thickness were chosen, namely 3, 1.5, and 1, and for each of these cases, multiple length to width ratios were chosen (Table 1). The length, width, and thickness were referred to as the size descriptors for cuboidal particles ordered from the largest to the smallest, which were called  $L_1$ ,  $L_2$ , and  $L_3$ , respectively, where  $L_1 > L_2 > L_3$ . The values of these ratios were selected to obtain different particle shapes, such as flat and elongated cuboids, to evaluate the effect on the accuracy of the measurement method.

### 2.1. Fabrication of the Cuboidal Analytical Standards

The particles were fabricated using standard photolithography (Figure 1). For each batch of particles, a thin layer of SU-8 (GM1070, Gersteltec Engineering Solutions, Switzerland) was spin coated on a silicon wafer. The spin coating

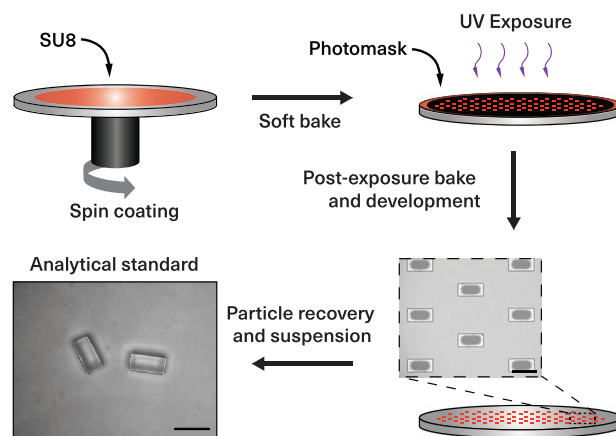


**Figure 1.** Fabrication of particles: a layer of SU-8 photoresist was spin coated on a silicon wafer. The photoresist was soft baked and exposed to UV through a photomask, leading to photopolymerization of the exposed parts. Afterwards, the resists was baked and developed to remove the unpolymerized SU-8. The resulting structures were gently scraped off the wafer and suspended in distilled water. (Scale: 200  $\mu\text{m}$ )

speed determines the thickness of the SU-8 layer on the wafer and was estimated from the SU-8 GM1070 datasheet. The SU-8 was allowed to rest for  $\approx 3$  h and, subsequently, soft baked for 2 min at 65  $^{\circ}\text{C}$  and 30 min at 95  $^{\circ}\text{C}$ . Afterwards, the SU-8 was exposed to UV through a high-resolution film photomask followed by baking at 95  $^{\circ}\text{C}$  for 15 min. Next, the features were developed by submerging the wafer in 2-(1-methoxy)propyl acetate (PGMEA 99%; Acros Organics, Geel, Belgium) and shaking gently. Details regarding the spin coating speed, exposure dose, and development time for different particle thicknesses are reported in Table 2. The wafer was carefully rinsed with fresh PGMEA and 2-propanol (IPA; Sigma-Aldrich, Steinheim, Germany) and blow-dried with nitrogen. To take the particles off the wafer, 1 mL of distilled water and IPA was dispensed on the wafer and the particles were brushed off gently using a PVDF (polyvinylidene fluoride)-tip tweezers (Ted Pella Inc., Redding, CA, USA). Particles were washed using distilled water and collected in a 50 mL centrifuge tube.

### 2.2. Preliminary Characterization of the Particles

A 3D Laser Scanning Microscope (Keyence VK-X100; Itasca, IL, USA) was used to measure the size of the particles when still on the wafer (column 2 of Table 3). The thinner platelets, corresponding to a higher  $L_2/L_3$  aspect ratio, were only slightly longer and wider than the design size, while the thicker platelets were up to  $\approx 5$   $\mu\text{m}$  longer and wider.

**Table 2.** Parameters of the photolithography process.

Particle thickness [ $\mu\text{m}$ ]	SU-8 spin coating speed [rpm]	Exposure dose [ $\text{mJ cm}^{-2}$ ]	Development time [min]
33	2500	620	3
66	1300	850	4
100	900	1000	5

**Table 3.** Measured average sizes and standard deviations.

Aspect ratio $L_2/L_3$		Real size [ $\mu\text{m}$ ]	Measured size ML [ $\mu\text{m}$ ]	Measured size OBB [ $\mu\text{m}$ ]
3	$L_1$	101	102 ± 9	117 ± 9
	$L_2$	101	93 ± 8	112 ± 8
	$L_3$	31	48 ± 16	73 ± 20
	$L_1$	202	205 ± 13	215 ± 12
	$L_2$	102	100 ± 10	121 ± 19
	$L_3$	32	45 ± 12	76 ± 22
	$L_1$	300	309 ± 12	316 ± 11
	$L_2$	102	105 ± 6	119 ± 19
	$L_3$	32	39 ± 11	70 ± 20
1.5	$L_1$	205	213 ± 12	226 ± 13
	$L_2$	105	114 ± 10	141 ± 23
	$L_3$	66	69 ± 14	104 ± 18
	$L_1$	306	313 ± 12	326 ± 16
	$L_2$	106	120 ± 9	142 ± 31
	$L_3$	66	66 ± 14	103 ± 18
	$L_1$	205	214 ± 12	230 ± 11
	$L_2$	105	130 ± 14	161 ± 28
	$L_3$	105	98 ± 15	136 ± 14
1	$L_1$	306	316 ± 12	330 ± 17
	$L_2$	110	135 ± 15	164 ± 37
	$L_3$	106	95 ± 14	139 ± 14

### 2.3. Sample Preparation

After production, the cuboidal particles suspended in distilled water were allowed to settle, and most of the liquid was removed with a syringe. The solvent composition was then adjusted to the following proportions: 36 mL deionized water (Milli-Q Advantage A10 system, Millipore, Zug, Switzerland), 12 mL IPA (ACS Reagent ≥ 99.8%, Sigma–Aldrich, Steinheim, Germany), and 2 mL 0.5 wt.% Pluronic F-127 (BioReagent, Sigma–Aldrich, Steinheim, Germany) aqueous solution. Compared to deionized water alone, IPA aids in submerging the particles by reducing surface tension. Pluronic F-127 was added to reduce particle aggregation.

### 2.4. Measurement with the Imaging Device

A simplified schematic of the measurement setup is shown in panel (a) of **Figure 2**. Each 50 mL suspension was pumped through the flow cell of the imaging device. Once the system had been degassed, measurement was started. The imaging device<sup>[39]</sup> consists of two 5 megapixel cameras equipped with telecentric lenses and arranged perpendicular to each other. The cameras are able to capture images of the flowing suspension simultaneously with a shutter speed of 6  $\mu\text{s}$ , thus yielding images virtually free of motion blur. The optical system has an object space resolution of 1  $\mu\text{m}$  and a field of view of 2.5 mm × 2.0 mm. Each measurement consisted of

9000 images per camera, collected at 75 Hz and processed in real time, taking a total of 10 min.

The raw images were processed to calculate the particle size and shape distributions using an IA algorithm described in detail elsewhere.<sup>[39]</sup> Briefly, for each particle, the contours were extracted and combined from the raw images captured by the two cameras, as shown in panel (b) of **Figure 2**. The approximate 3D shape of each particle is given by the visual hull obtained using shape-from-silhouette reconstruction. As described extensively elsewhere, the success of this approach is dependent on the viewing directions, here fixed, and on the particle orientation.<sup>[6,45]</sup> This issue is exemplified in panels (b) and (c) of **Figure 2**: one platelet is favorably aligned, that is, its faces are orthogonal to the imaging planes, while the other is unfavorably aligned. Upon 3D reconstruction, the first one matches the real particle shape, that is, a cuboid sized 202 × 102 × 32  $\mu\text{m}$ , while the second is rendered as a thick rhomboid.

Based solely on the reconstructed 3D particle shape, the sizing method of choice was the optimal fitting of an oriented bounding box (OBB),<sup>[46]</sup> displayed in red in panel (c) of **Figure 2**. By applying this method, the favorably aligned platelet was sized 213 × 108 × 48  $\mu\text{m}$ , while the unfavorably aligned one was sized 229 × 151 × 101  $\mu\text{m}$ . As a replacement of the OBB method, the machine learning (ML) algorithm presented elsewhere was used.<sup>[40]</sup> It consists of an artificial neural network with two layers and 50 nodes in each layer, trained on data generated using a simulation tool that replicates the functioning of the imaging device. As schematized in panel (d) of **Figure 2**, the artificial neural network took as input for each particle both 2D and 3D features and output its predicted length, width, and thickness. 2D features were extracted from the contours, while 3D features were extracted from the 3D reconstructed particle.<sup>[39]</sup> By employing this algorithm, the favorably aligned platelet was sized 215 × 98 × 39  $\mu\text{m}$ , while the unfavorably aligned one was sized 200 × 98 × 58  $\mu\text{m}$ .

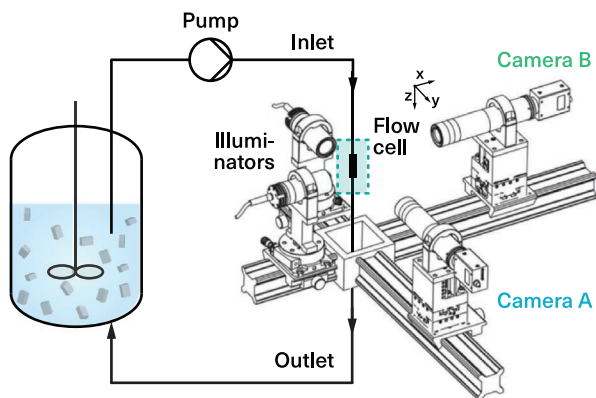
Finally, to generate the particle size distributions discussed next, a set of outliers (such as bubbles, dust particles, or broken particles) was detected from the particle list and removed. Further details about outlier removal procedures are provided in the Supporting Information.

## 3. Results and Discussion

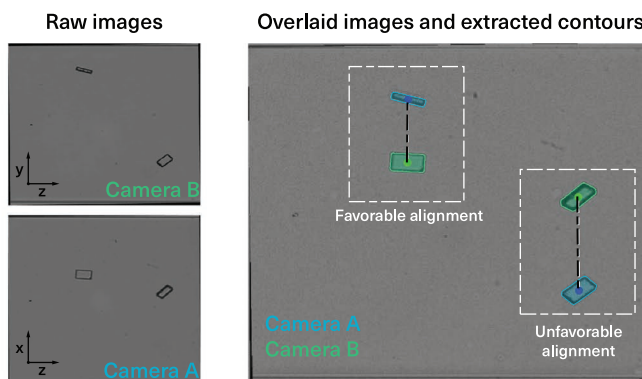
### 3.1. 3D Particle Size and Shape Distributions

For each population, both image processing algorithms (OBB and ML) resulted in a  $N \times 3$  matrix, where  $N$  is the number of particles measured by the device, varying between 5000 and 10 000, with 3 being the number of characteristic lengths. Each data set is binned with a fixed bin width of 4  $\mu\text{m}$  to yield a 3D particle size and shape distribution (3D PSSD)  $f(L_1, L_2, L_3)$ . Since  $f: \mathbb{R}^{+3} \rightarrow \mathbb{R}_0^+$  cannot be graphed directly, three isosurfaces are plotted in 3D space, enclosing 25%, 50%, and 80% of constituent particles in the distribution. The 3D PSSDs of the populations with different aspect ratios  $L_2/L_3$ , that is, 3, 1.5, and 1, computed using the ML model, are shown on the left-hand-side of panels (a), (b), and (c) of **Figure 3**, respectively. The

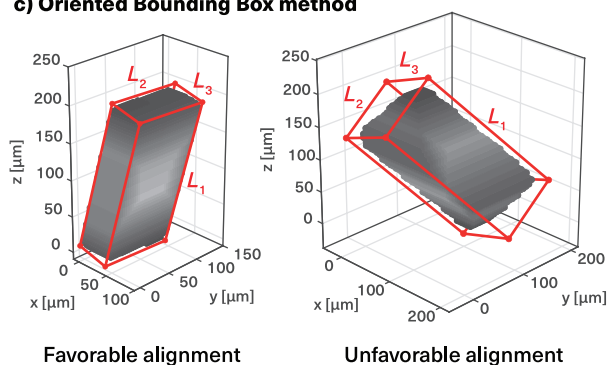
a) Measurement setup



b) Imaging, contour extraction, and matching



c) Oriented Bounding Box method



d) Machine learning algorithm approach

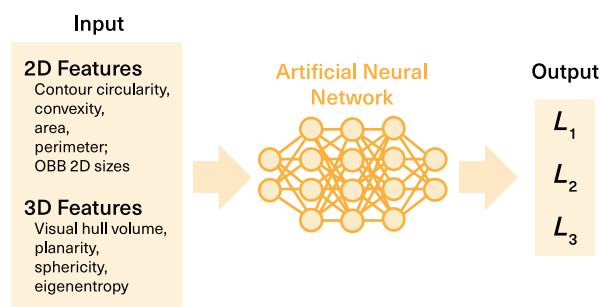


**Figure 2.** a) Visualization of the measurement setup. Adapted with permission under the terms of the Creative Commons CC BY license from ref. [39]. Copyright 2017, the Authors. Published by Elsevier B.V. b) Example of two images collected simultaneously from camera A and B. The IA algorithm extracts the contours and, subsequently, matches the particles captured in the two images. Due to the fact that particles rotate as they flow, alignment may not be always favorable for measurement with the optical system. c) Rendering of the visual hull of the two particles shown in (b) obtained by shape-from-silhouette 3D reconstruction. While the two particles have the same size in reality ( $202 \times 102 \times 32 \mu\text{m}$ ), the visual hulls are very different due to the particle orientation. Upon fitting an oriented bounding box (shown in red), the characteristic lengths are computed. The OBB estimates  $213 \times 108 \times 48 \mu\text{m}$  for the favorably aligned particle and  $229 \times 151 \times 101 \mu\text{m}$  for the unfavorably aligned. d) Visualization of the inputs and outputs of the ML model, which yields  $215 \times 98 \times 39 \mu\text{m}$  for the favorably aligned particle and  $200 \times 98 \times 58 \mu\text{m}$  for the unfavorably aligned.

3D PSSDs visually appear as “blobs” made of the three nested isosurfaces. The innermost shell, having a darker color shade, contains 25% of the total number of particles in the distribution closest to its maximum, while the outermost shell with a lighter shade contains 80% thereof. This mode of visualization allows us to comparatively evaluate the shape of the distribution and its compactness. Furthermore, dimensionality reduction is applied by plotting the three 2D marginal distributions

$$f_{L_1, L_2}, f_{L_1, L_3}, \text{ and } f_{L_2, L_3}, \text{ defined as } f_{L_i, L_j} = \int_0^\infty f dL_k, \text{ interpreted as}$$

projections of the 3D PSSD onto the hyperplanes. The 2D marginal distributions are visualized as contour plots with three contour lines each, computed to enclose 25%, 50%, and 80% of the total number of particles. Let us consider the 3D PSSD on the left-hand-side of panel (a) of Figure 3. The distributions of the populations with approximate length 300, 200, and  $100 \mu\text{m}$ , width  $100 \mu\text{m}$ , and thickness  $33 \mu\text{m}$  are shown. Qualitatively, the distributions are monomodal and centered around the real size. This is especially evident when considering the  $(L_1, L_2)$  and  $(L_2, L_3)$  planes. On the  $(L_1, L_2)$  plane, it can be clearly seen that the three marginal distributions are

centered around  $L_2 = 100 \mu\text{m}$  and that  $L_1$  varies between 100 and  $300 \mu\text{m}$ . While, on the  $(L_2, L_3)$  plane, the distributions overlap since  $L_2$  and  $L_3$  are the same for all three populations. These considerations relate to the measurement accuracy. Assuming perfect monodispersity of the analyzed particles, the 3D PSSD should be a point in the space. Due to a number of unavoidable effects, for instance the variable particle orientation, which affects the reconstructed visual hull, and optical limitations of the imaging setup, the observed 3D PSSD shows a finite broadness,<sup>[40]</sup> which relates to the intrinsic limitations in the measurement precision.

3.2. Numerical Results

For the ML model, the measured average sizes and standard deviations of all populations are reported in the third column of Table 3. The measured average lengths and widths differ on average by 3% and 12% (7 and  $12 \mu\text{m}$  absolute) from the real values, respectively, while the estimate of the thickness is subject to a larger relative error, depending on the absolute size, of 20% on average ( $8 \mu\text{m}$  absolute). The error is more pronounced for thinner platelets,

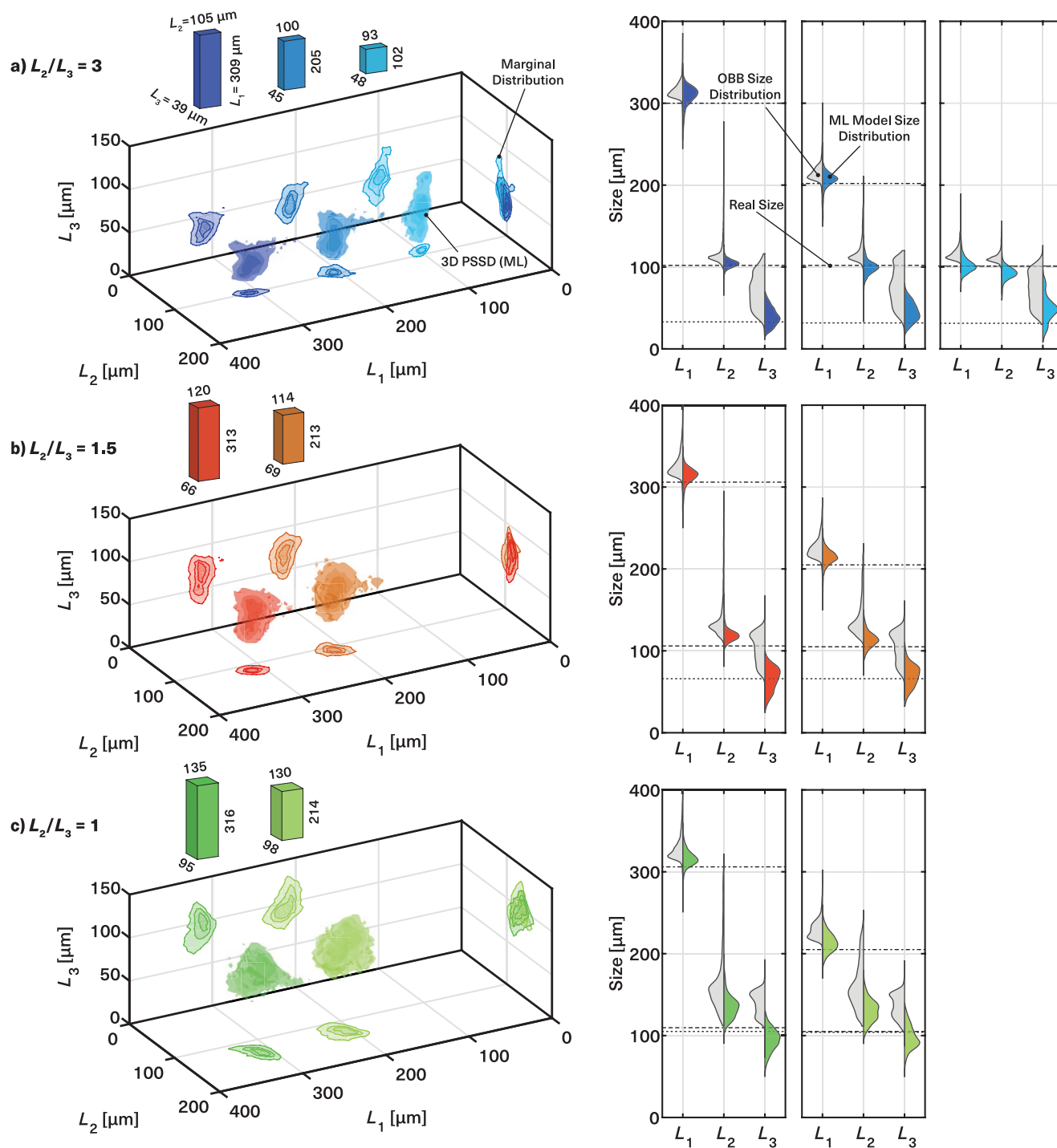


**Figure 3.** Left-hand-side: 3D particle size and shape distributions (3D PSSDs) obtained using the ML model. The results for aspect ratios  $L_2/L_3$  3, 1.5, and 1 are shown in panels (a), (b), and (c), respectively. On top of each plot, the average measured values are shown next to the thumbnails of the particles. On the right-hand-side, violin plots corresponding to the three 1D marginal distributions obtained using the OBB model (gray half) and ML model (colored half) are demonstrated. The horizontal lines represent the real size of the particles; the dash-dotted lines, dashed lines, and dotted lines represent  $L_1$ ,  $L_2$ , and  $L_3$ , respectively.

which are harder to size due to the more adverse effects of particle orientation on measurement accuracy, as extensively shown in prior research.<sup>[40]</sup> The standard deviations were observed to be at most 16  $\mu\text{m}$  for all characteristic lengths and among all the

investigated populations, which is a positive indication that the precision of the measurement is reasonably scale-independent.

The device and its measurement pipeline tend to overestimate all characteristic lengths. This behavior can be explained

by considering two factors. First, the area and the perimeter of the projected contours and, in turn, of the shape-from-silhouette 3D reconstruction, yield an upper bound on the true 3D shape of the imaged object.<sup>[47]</sup> Second, the telecentric lenses used by the device have a shallow depth of field; hence, in every snapshot, not all the particles are in perfect focus; the resulting blur, in the current implementation of the IA algorithm, which employs fixed-level binary thresholding, leads to larger contours. Measurements with monodisperse latex beads and optical patterns allowed us to estimate that the latter effect accounts for deviations up to 5  $\mu\text{m}$ . In spite of this, interestingly, in three instances, the characteristic length is visibly underestimated, namely  $L_2$  of the first population and  $L_3$  of the last and second last populations. This effect is due to the inability of the device to distinguish the faces of the particles. The three values obtained from the ML model or OBB method, in fact, cannot be uniquely assigned to each of the three geometrical characteristic lengths. Thus, their sorting is accomplished based on the assumption that the largest observed value corresponds to  $L_1$ , the middle one to  $L_2$ , and the smallest one to  $L_3$ . Consequently, if two characteristic lengths happen to be very similar, say  $L_2$  and  $L_3$  as in the two latter cases, upon measuring, above-average values will be mostly assigned to  $L_2$ , while below-average values will be mostly assigned to  $L_3$ . Thus,  $L_3$  will be underestimated while  $L_2$  will be overestimated. More advanced clustering techniques could help reduce this bias, but their investigation is beyond the scope of this article.

### 3.3. Comparison Between the OBB method and ML model

The comparison of results presented in the previous sections with the results obtained with the OBB method is made based on the numeric values (last column of Table 3), 3D PSSDs (Figure S3 in the Supporting Information), and its marginal distributions. The average sizes computed with the OBB method are worse for any characteristic length and population; the measured average lengths, widths, and thicknesses differ in relative terms on average by 9%, 30%, and 80% (19, 33, and 38  $\mu\text{m}$  absolute) from the real values, respectively. The standard deviations are up to 37  $\mu\text{m}$  and likewise higher compared to the ML model, particularly for the particle width  $L_2$  at larger values of  $L_3$ . This is attributed to the effect of particle orientation, which is further elucidated through simulations.<sup>[40]</sup>

Visually, the different outputs of the two methods can be appreciated by means of violin plots, shown on the right-hand-side of panels (a), (b), and (c) of Figure 3. Violin plots are useful graphical tools to display the density distributions in a compact fashion, thus allowing a rapid comparison among distributions. Three violin plots are displayed in each subfigure; each violin shows the 1D marginal distribution  $f_{L_i} = \int_0^{\infty} \int_0^{\infty} f dL_j dL_k$  from the OBB method, on its left side and in gray, and from the ML model, on its right side and using the same color code as in the 3D PSSDs. The horizontal lines represent the real characteristic lengths. As already indicated in Table 3, the OBB distributions visibly suffer from a greater offset and variance, particularly for the particles' thickness  $L_3$ . Finally, inspection of the 3D PSSDs (Supporting Information) reveals that the distributions with the

OBB method are considerably less compact, and local maxima are visible in the marginal distributions. This is especially unfavorable when dealing with real polydisperse populations, since it can lead to incorrect conclusions upon clustering.

### 3.4. Estimating the Particle Orientation

The two projected images of each particle can also be used to infer their orientation in the flow cell. This is achieved by optimizing the orientation of a simulated cuboid, with the target of matching its projections to those observed in the real images. Using this procedure, which is described in detail in the Supporting Information, a distribution of orientations is obtained for each particle population. To analyze such distributions, two physically meaningful angles are extracted from each orientation, namely  $\theta$  and  $\phi$ , which describe particle alignment with respect to the flow direction (Figure 4).  $\theta$  is defined as the angle between the flow direction and the vector normal

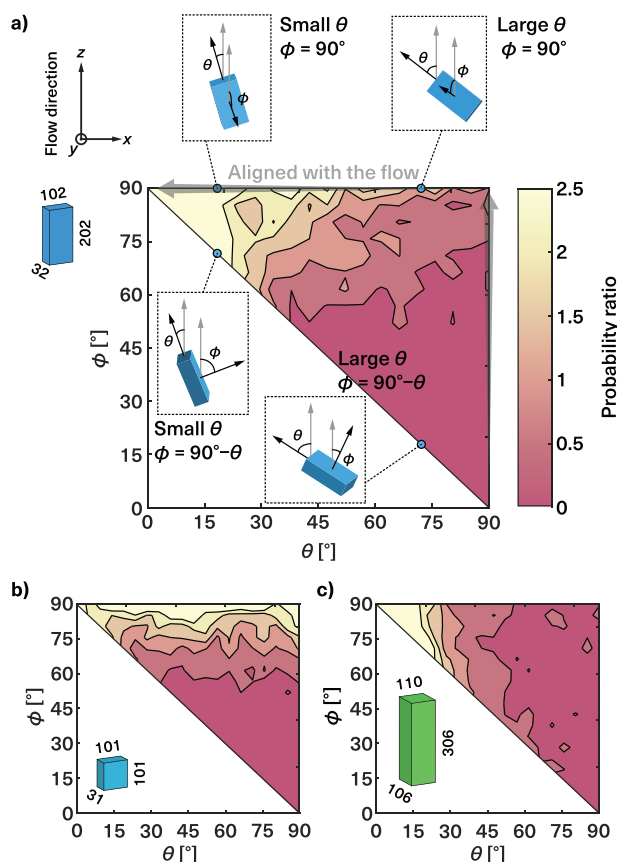


**Figure 4.** Distributions of  $\theta$  and  $\phi$  normalized with respect to uniformly random orientation distribution. Panel (a) shows the distribution obtained from images of the particles with size  $202 \times 102 \times 32 \mu\text{m}$ , panel (b) of particles with size  $101 \times 101 \times 31 \mu\text{m}$ , and panel (c) of particles with size  $306 \times 110 \times 106 \mu\text{m}$ . Panel (a) additionally contains examples of cuboids aligned with different combinations of  $\theta$  and  $\phi$  (dotted boxes), with their position in the  $(\theta - \phi)$  plane marked accordingly (blue dots). In the aforementioned examples, the gray arrows represents the flow direction, while the black arrows represent the vectors normal to the the smallest and largest face of the particle, from which the angles are measured.

to the smallest face of the particle, that is, the face spanned by  $L_2$  and  $L_3$ .  $\phi$  is defined as the angle between the flow direction and the vector normal to the largest face of the particle, that is, the face spanned by  $L_1$  and  $L_2$ . Due to the symmetry of the cuboids, there are three pairs of faces. For both angles  $\theta$  and  $\phi$ , the face leading to a smaller angle is chosen. This implies that  $0^\circ < \theta < 90^\circ$  and, for a given  $\theta$ ,  $90^\circ - \theta < \phi < 90^\circ$ . The angle  $\theta$  sets a boundary to the values of  $\phi$  that can be reached because the vectors normal to the faces of a cuboid are perpendicular to each other. Therefore, fixing one of the normal vectors constrains the direction of the other two.

The probability density functions of these two angles for three exemplary particle populations are shown in panels (a–c) of Figure 4. The remaining set of distributions is provided in the Supporting Information. It can be shown that a uniform distribution of orientations in the 3D space does not lead to a uniform distribution of  $\theta$  and  $\phi$ . Hence, to enable an immediate comparison against the random orientation case, the distributions obtained experimentally have to be normalized by the distribution of  $\theta$  and  $\phi$  corresponding to uniformly distributed orientations, which is derived in the Supporting Information. The resulting quantity is here referred to as the probability ratio. Combinations of angles having a probability ratio greater than 1 are more likely compared to the random case, while the opposite holds for a probability ratio  $< 1$ .

It is evident from Figure 4 that the particle shape affects the orientation distribution. Panel (b) shows that flat cuboids with  $L_1 = L_2 > L_3$  preferentially align with the vector normal to their largest face perpendicular to the flow ( $\phi \approx 90^\circ$ ), while seemingly having no preference in  $\theta$ . Panel (c) shows that cuboids with  $L_1 > L_2 = L_3$  preferentially align with the vector normal to their smallest face parallel the flow ( $\theta \approx 0^\circ$ ), while seemingly having no preference in  $\phi$ . Finally, in panel (a), it can be observed that cuboids with three different characteristic lengths exhibit a combination of the previously described preferential orientations, that is,  $\theta \approx 0^\circ$  and  $\phi \approx 90^\circ$ .

Considering the orientation distributions of all particle populations (Supporting Information), we report that the alignment becomes more biased compared to the random orientation case at higher aspect ratios. In particular, the results suggest that more elongated particles preferentially orient themselves with their major axis parallel to the direction of fluid flow, which matches previous works.<sup>[41,44,48]</sup> Flatter particles however tend to align with their largest face parallel to the flow. Thus, the alignment of elongated particles can be largely described by  $\theta$  alone, while the alignment of flat particles is majorly related to  $\phi$ . Particles that are both flattened and elongated exhibit preferential orientation based on a combination of both angles.

The results presented above, and obtained under laminar flow conditions ( $Re \approx 300$ ), are consistent with findings reported in the literature.<sup>[44,49–51]</sup> Given the relevance of the topic, which has been the object of extensive investigation both numerically and experimentally,<sup>[41,43,44,48,51–54]</sup> the method presented in this contribution can be potentially useful to a broad end-user group, specifically in the computational fluid dynamics community, to conduct systematic studies on particle-laden flows.

## 4. Conclusions

Based on the experimental findings discussed herein, the outcomes of this work can be summarized as follows:

- Cuboidal particles have been fabricated through photolithography and used as monodisperse analytical standards, thus enabling the validation of a particle size and shape measurement technique based on multiprojection imaging coupled with a machine learning model. Thanks to its accuracy and flexibility, the proposed fabrication technique is a valuable tool for producing particles of controlled sizes and shapes, which will be of high interest in the particle technology space.
- Multiprojection imaging coupled with machine learning yields accurate estimates of the three characteristic lengths of ensembles of cuboidal particles. Further, in contrast to other sizing techniques, it is able to perform measurements in real-time and in flow. The quality of the measurements highlights the reliability of the measurement technique, and is indicated by the low measurement error and its standard deviation, which are both of the order of  $10 \mu\text{m}$  for all three characteristic lengths and all the populations considered here.
- The set of images collected during analysis can be used to obtain an estimate of the particles' orientation in the flow, providing a potentially useful experimental technique to support computational results obtained from multiphase fluid dynamics simulations.

## Supporting Information

Supporting Information is available from the Wiley Online Library or from the author.

## Conflict of Interest

The authors declare no conflict of interest.

## Author Contributions

P.B., A. Jaeggi, and A.K.R. designed research; A. Jain fabricated the microparticles; P.B. and A. Jaeggi performed research; P.B., A. Jaeggi, and D.B. analyzed data; P.B., A. Jain, and A. Jaeggi wrote the paper; A.K.R., A.J.d., and M.M. supervised the work.

## Data Availability Statement

The data that support the findings of this study are openly available in LithoPlatelets at 10.5281/zenodo.7215090, reference number 7215090.

## Keywords

3D characterization, 3D imaging, analytical standards, particle orientation, photolithography

Received: August 4, 2022  
Revised: October 19, 2022  
Published online:

- [1] G. Patience, M. Rigamonti, H. Li, in *Experimental Methods and Instrumentation for Chemical Engineers*, chapter 10, 2nd ed., Elsevier, Amsterdam **2018**, pp. 293–338.
- [2] W. Yu, L. Liao, R. Bharadwaj, B. C. Hancock, *Powder Technol.* **2017**, 313, 1.
- [3] I. de Albuquerque, M. Mazzotti, D. R. Ochsenein, M. Morari, *AIChE J.* **2016**, 62, 2974.
- [4] A. Tinke, A. Carnicer, R. Govoreanu, G. Scheltjens, L. Lauwerysen, N. Mertens, K. Vanhoutte, M. Brewster, *Powder Technol.* **2008**, 186, 154.
- [5] A. Califice, F. Michel, G. Dislaire, E. Pirard, *Powder Technol.* **2013**, 237, 67.
- [6] X. Jia, E. J. Garboczi, *Particuology* **2016**, 26, 19.
- [7] E. Pirard, *Image Analysis and Stereology* **2012**, 31, 65.
- [8] D. L. Galata, L. A. Mészáros, N. Kállai-Szabó, E. Szabó, H. Pataki, G. Marosi, Z. K. Nagy, *Eur. J. Pharm. Sci.* **2021**, 159, January.
- [9] D. M. Scott, *Powder Technol.* **2022**, 399, 117159.
- [10] S. A. Schiele, R. Hupfer, F. Luxenburger, H. Briesen, *Cryst. Growth Des.* **2021**, 21, 6373.
- [11] S. A. Schiele, F. Antoni, R. Meinhardt, H. Briesen, *Cryst. Growth Des.* **2021**, 21, 1751.
- [12] T. D. Turner, P. Gajjar, I. S. Fragkopoulos, J. Carr, T. T. H. Nguyen, D. Hooper, F. Clarke, N. Dawson, P. J. Withers, K. J. Roberts, *Cryst. Growth Des.* **2020**, 20, 4252.
- [13] X. Z. Wang, K. J. Roberts, C. Ma, *Chem. Eng. Sci.* **2008**, 63, 1173.
- [14] T. Kovačević, A. Reinhold, H. Briesen, *Cryst. Growth Des.* **2014**, 14, 1666.
- [15] T. Kovačević, J. Schock, F. Pfeiffer, H. Briesen, *Cryst. Growth Des.* **2016**, 16, 2685.
- [16] B. Zhao, J. Wang, *Powder Technol.* **2016**, 291, 262.
- [17] C. L. Lin, J. D. Miller, *Powder Technol.* **2005**, 154, 61.
- [18] S. Shao, K. Mallery, J. Hong, *Chem. Eng. Sci.* **2020**, 225, 115830.
- [19] T. Khanam, A. Rajendran, V. Kariwala, A. K. Asundi, *Cryst. Growth Des.* **2013**, 13, 3969.
- [20] E. Darakis, T. Khanam, A. Rajendran, V. Kariwala, T. J. Naughton, A. K. Asundi, *Chem. Eng. Sci.* **2010**, 65, 1037.
- [21] Q. Sun, Y. Zheng, B. Li, J. Zheng, Z. Wang, *Geotechnique Lett.* **2019**, 9, 72.
- [22] C. Borchert, E. Temmel, H. Eischmidt, H. Lorenz, A. Seidel-Morgenstern, K. Sundmacher, *Cryst. Growth Des.* **2014**, 14, 952.
- [23] O. S. Agimelen, A. Jawor-Baczynska, J. McGinty, J. Dziejewicz, C. Tachtatzis, A. Cleary, I. Haley, C. Michie, I. Andonovic, J. Sefcik, A. J. Mulholland, *Chem. Eng. Sci.* **2016**, 144, 87.
- [24] S. Schorsch, J.-H. Hours, T. Vetter, M. Mazzotti, C. N. Jones, *Comput. Chem. Eng.* **2015**, 75, 171.
- [25] R. Zhang, C. Y. Ma, J. J. Liu, X. Z. Wang, *Chem. Eng. Sci.* **2015**, 137, 9.
- [26] J. Calderon De Anda, X. Wang, K. Roberts, *Chem. Eng. Sci.* **2005**, 60, 1053.
- [27] R. F. Li, G. B. Thomson, G. White, X. Z. Wang, J. C. De Anda, K. J. Roberts, *AIChE J.* **2006**, 52, 2297.
- [28] B. Bujak, M. Bottlinger, *Part. Part. Syst. Character.* **2008**, 25, 293.
- [29] S. Schorsch, D. R. Ochsenein, T. Vetter, M. Morari, M. Mazzotti, *Chem. Eng. Sci.* **2014**, 105, 155.
- [30] M. Oullion, F. Puel, G. Févotte, S. Righini, P. Carvin, *Chem. Eng. Sci.* **2007**, 62, 820.
- [31] P. Neoptolemos, N. Goyal, A. J. Cruz-Cabeza, A. A. Kiss, D. J. Milne, T. Vetter, *Powder Technol.* **2022**, 399, 116827.
- [32] M. R. Singh, J. Chakraborty, N. Nere, H.-H. Tung, S. Bordawekar, D. Ramkrishna, *Cryst. Growth Des.* **2012**, 12, 3735.
- [33] I. Soppela, S. Airaksinen, J. Hatara, H. Rääkkönen, O. Antikainen, J. Yliruusi, N. Sandler, *AAPS PharmSciTech* **2011**, 12, 476.
- [34] J. Cardona, C. Ferreira, J. McGinty, A. Hamilton, O. S. Agimelen, A. Cleary, B. Atkinson, C. Michie, S. Marshall, Y.-C. Chen, J. Sefcik, I. Andonovic, C. Tachtatzis, *Chem. Eng. Sci.* **2018**, 191, 208.
- [35] P. Neugebauer, J. Cardona, M. O. Besenhard, A. Peter, H. Gruber-Woelfler, C. Tachtatzis, A. Cleary, I. Andonovic, J. Sefcik, J. G. Khinast, *Cryst. Growth Des.* **2018**, 18, 4403.
- [36] S. Bötschi, A. K. Rajagopalan, I. Rombaut, M. Morari, M. Mazzotti, *Comput. Chem. Eng.* **2019**, 131, 106581.
- [37] A. Eren, B. Szilagyi, J. L. Quon, C. D. Papageorgiou, Z. K. Nagy, *Cryst. Growth Des.* **2021**, 21, 3981.
- [38] C. A. Offiler, A. J. Cruz-Cabeza, R. J. Davey, T. Vetter, *Cryst. Growth Des.* **2021**, acs.cgd.1c01019.
- [39] A. K. Rajagopalan, J. Schneeberger, F. Salvatori, S. Bötschi, D. R. Ochsenein, M. R. Oswald, M. Pollefeys, M. Mazzotti, *Powder Technol.* **2017**, 321, 479.
- [40] A. Jaeggi, A. K. Rajagopalan, M. Morari, M. Mazzotti, *Ind. Eng. Chem. Res.* **2021**, 60, 473.
- [41] V. V. Mahajan, J. T. Padding, T. M. Nijssen, K. A. Buist, J. A. Kuipers, *AIChE J.* **2018**, 64, 1573.
- [42] T. Dabat, F. Hubert, E. Paineau, P. Launois, C. Laforest, B. Grégoire, B. Dazas, E. Tertre, A. Delville, E. Ferrage, *Nat. Commun.* **2019**, 10, 1.
- [43] M. Trebbin, D. Steinhauser, J. Perlich, A. Buffet, S. V. Roth, W. Zimmermann, J. Thiele, S. Förster, *Proc. Natl. Acad. Sci. USA* **2013**, 110, 6706.
- [44] M. Mandø, C. Yin, H. Sørensen, L. Rosendahl, in *Proceedings of the ICMF 2007, 6th International Conference on Multiphase Flow*, Leipzig, Germany **2007**.
- [45] K. Shanmukh, A. K. Pujari, *Pattern Recognition Letters* **1991**, 12, 165.
- [46] J. Korsawe, Minimal Bounding Box, **2022**, <https://www.mathworks.com/matlabcentral/fileexchange/18264-minimal-bounding-box> (accessed: October 2019).
- [47] A. Laurentini, *IEEE Transactions on Pattern Analysis and Machine Intelligence* **1994**, 16, 150.
- [48] O. Bernstein, M. Shapiro, *J. Aerosol Sci.* **1994**, 25, 113.
- [49] G. B. Jeffery, *Proceedings of the Royal Society of London. Series A, Containing Papers of a Mathematical and Physical Character* **1922**, 102, 161.
- [50] L. Jianzhong, Z. Weifeng, Y. Zhaosheng, *J. Aerosol Sci.* **2004**, 35, 63.
- [51] C. A. Stover, C. Cohen, *Rheol. Acta* **1990**, 29, 192.
- [52] M. Z. Sheikh, K. Gustavsson, D. Lopez, E. Lévêque, B. Mehlig, A. Pumir, A. Naso, *Journal of Fluid Mechanics* **2020**, 886, A9.
- [53] D. Vincenzi, *Journal of Fluid Mechanics* **2013**, 719, 465.
- [54] D. Gunes, R. Scirocco, J. Mewis, J. Vermant, *J. Non-Newtonian Fluid Mech.* **2008**, 155, 39.